Nuclear Instruments and Methods in Physics Research A 1090 (2026) 171676

Contents lists available at ScienceDirect

Nuclear Inst. and Methods in Physics Research, A

journal homepage: www.elsevier.com/locate/nima

Full Length Article

From charge tracking to signal formation: A multi-body approach for simulating Coulomb effects in semiconductor detectors

Pietro Zambon [a,*], Filippo Buda [b], Chiara Guazzoni [b,c], Andrea Castoldi [b,c]

[a] *DECTRIS Ltd., Taefernweg 1, Baden-Daettwil, 5405, Switzerland*
[b] *Dipartimento di Elettronica, Informazione e Bioingegneria (DEIB), Politecnico di Milano, Piazza Leonardo da Vinci 32, Milano, 20133, Italy*
[c] *INFN - Sezione di Milano, Via Celoria 16, Milano, 20133, Italy*

ARTICLE INFO

Keywords:
Semiconductor detector simulation
Signal formation
Charge tracking
Plasma effect
Monte Carlo simulation
Coulomb interaction

ABSTRACT

We present a simulation code for the solution of the electron–hole dynamics and signal formation in 3D semiconductor radiation detectors. The code adopts a multi-body approach, i.e. the evolution and interaction of the charge cloud is tracked on an individual carrier basis, using a combination of numerical ODE solvers and Monte Carlo methods. Particular emphasis is devoted to the treatment of the Coulomb interaction, critical for the correct simulation of high-density ionization tracks. This multi-body approach sheds light on the phenomenology of the plasma effect, revealing the underlying co-dependence between local field screening and carrier binding. In addition, a dynamic time-step algorithm allows for accurate tracking at virtually any time scale within accessible computational times. By nature, the problem makes the code architecture ideal for GPU-based parallel computing. The method is validated through comparison with experimental data from a p^{+}nn^{+} silicon diode under different bias and charge injection conditions representative of realistic scenarios encountered in modern X-ray facilities e.g. FELs.

1. Introduction

Numerical simulations are a fundamental tool in the field of detector science to accelerate the design of optimized structures and to gain better understanding of the physical mechanisms underlying the carrier dynamics and signal formation. The wide range of charge-injection levels expected at modern experimental facilities poses, however, non-trivial numerical challenges. In particular, the Coulomb interactions between carriers, responsible for the emergence of plasma effects especially during the first instants of the carriers dynamics, deserve accurate modeling. The strong mutual electrostatic forces can, indeed, result in an effective shielding of the core of the charge cloud from applied bias field, significantly slowing down their collection and degrading the response linearity with respect to the intensity of the impinging radiation. For example, the charge-injection levels at modern X-ray Free Electron Laser (FEL) facilities are as high as $3 \cdot 10^{7}$ e–h pairs ($10^{5} \cdot 12$ keV photons), concentrated in femtosecond pulses with physical size smaller than one pixel [1], can lead to severe distortions and delays of the readout current signals. In nuclear physics experiments, highly-segmented monolithic detector arrays feature a signal complexity at high charge-injection levels that must be carefully studied in order to optimize pulse-shape analysis techniques [2]. Further, as highlighted in recent reviews on future collider challenges [3], the next generation of high-energy physics (HEP) detectors will require timing resolutions in the order of tens of picoseconds. Reaching such precision demands simulation physics models with improved accuracy, also in view of novel materials such as low-gain avalanche diodes (LGAD). In this context, accounting for the plasma effect and related gain suppression mechanisms becomes critical to minimize systematic uncertainties in track and vertex reconstruction [4,5].

The insurgence of plasma effect has been a known phenomenon since the 1960s and 1970s, originally identified during the study of fission fragments [6,7]. A first coherent phenomenological description of the underlying mechanism was subsequently established in the pioneering works of Tove and Seibt [6,8], who characterized the process as a space-charge limited erosion of the ionized track. While these early models provided a fundamental analytical framework, the extreme charge densities encountered in modern experiments demand a transition from phenomenological approximations to fully self-consistent microscopic simulations. Existing simulation strategies can be broadly categorized into two groups: Monte Carlo frameworks for individual carrier tracking and mesh-based TCAD solvers based on continuum mechanics. Among the firsts, current simulation frameworks like

---

* Corresponding author.
E-mail addresses: pietro.zambon@dectris.com (P. Zambon), filippo.buda@mail.polimi.it (F. Buda), Chiara.Guazzoni@mi.infn.it (C. Guazzoni), Andrea.Castoldi@polimi.it (A. Castoldi).

https://doi.org/10.1016/j.nima.2026.171676
Received 20 March 2026; Received in revised form 12 May 2026; Accepted 12 May 2026

Garfield++ [9] and Allpix^2 [10], despite having become the standard for modeling silicon detectors in the high-energy physics community thanks to their modularity and efficiency, lack the computation of the Coulomb interaction between the carriers and therefore the capability to track space-charge induced effects. On the other hand, powerful commercial TCAD solvers, e.g., Synopsys Sentaurus [11] and Silvaco ATLAS [12], or custom-developed dedicated solutions [13–15], address the mutual interaction by solving the Poisson and continuity equations on a discrete mesh. For instance, 1D TCAD codes have been proposed that attempt to compensate for reduced dimensionality by adding analytical transverse ambipolar diffusion terms to model track expansion [13]. Other approaches employ nested mesh systems to improve computational efficiency on CPUs by refining the grid only in high-charge density regions [14]. Although these tools can model complex space-charge effects, such as gain suppression in LGADs [15], they treat the charge as continuous densities. Consequently, the physics is spatially averaged over the mesh cells, thus missing the discrete nature of the microscopic binding forces and local fluctuations at the basis of plasma formation and erosion. Furthermore, recent GPU-accelerated Monte Carlo methods, developed in the frame of Allpix^2, have been proposed to model charge repulsion, primarily focusing on large-scale event generation for detector calibration [16]. To maintain computational efficiency, these approaches often rely on simplified spherical symmetry assumptions for the charge cloud or employ statistical parameterizations to predict the final carrier distributions. Additionally, such models frequently adopt simplified analytical approximations for the drift electric field. While effective for spatial resolution studies, these simplifications can limit the accuracy in capturing the complex, non-isotropic dynamics of plasma separation and the resulting time-resolved induced signals.

Our contribution builds upon previous works [17–19] and focuses on the development of a Monte Carlo simulation code for the self-consistent computation of the electron–hole dynamics and signal formation in 3D semiconductor radiation detectors. Unlike grid-based methods, our code adopts a multi-body approach and tracks the spatio-temporal evolution of the charge cloud on an individual carrier basis, capturing the discrete Coulomb interactions that lead to space-charge effects. Since the complexity of the problem scales with $O(N^2)$, several numerical strategies were implemented to optimize the computational effort. First, the number of carriers can be reduced via charge clustering, each cluster having a correspondingly higher effective charge. Second, the simulation time step is adjusted at run-time as a function of a maximum allowable carrier displacement. Thus, the charge dynamics are tracked with great accuracy across virtually any time scale without significant impact on the overall computation time. The inherently parallel nature of the carrier tracking algorithm makes it perfectly suited for GPU acceleration, enabling the efficient handling of large-scale multi-body interactions.

The code was validated through comparison with experimental data on a p$^+$nn$^+$ silicon diode under different bias conditions and realistic charge injections up to 10^7 e–h pairs, representative of the realistic operating conditions at X-ray facilities e.g. FELs. This scenario mimics the one described in the work of Becker [20] which provides a fundamental benchmark for understanding how massive charge injection at FELs leads to intensity-dependent pulse distortions. Detailed analysis on the electric fields acting on the carriers emphasize the interplay between external field screening and internal Coulomb contributions, shedding light on the exact mechanisms that govern carrier separation in ultra-dense ionization tracks.

2. Materials and methods

2.1. Physical model

The simulated scenario consists of a 3D volume representing a fully-depleted semiconductor radiation detector. The volume hosts a static electric field which is defined by the boundary conditions at the domain walls in all three dimensions and by the fixed charges possibly contained within the volume itself. A 3D electron–hole charge cloud is given as input parameter, specifying the position and charge value of each individual carrier. The total field acting on the ith carrier is obtained as a superposition of the static term and a time-dependent term arising from the mutual Coulomb interaction with the surrounding jth mobile carriers:

$$\mathbf{E}_{\mathrm{tot}_i}\left(\mathbf{r}_1(t),\mathbf{r}_2(t),\ldots,\mathbf{r}_N(t)\right)=\mathbf{E}_{\mathrm{stat}_i}\left(\mathbf{r}_i(t)\right)+\sum_{j=1}^{N}\mathbf{E}_{\mathrm{mob}_{i\leftarrow j}}\left(\mathbf{r}_i(t),\mathbf{r}_j(t)\right) \tag{1}$$

where $\mathbf{r}(t)$ represent the position vector of the corresponding carrier, in general a function of time, and N corresponds to the total number of carriers in the domain. The functional dependence of $\mathbf{E}_{\mathrm{tot}}$ on the position of each carrier stems from the relative motion of the surrounding mobile carriers through $\mathbf{E}_{\mathrm{mob}_{i\leftarrow j}}$. The calculation of this last term is not limited to the direct line-of-sight interaction between charges, but it is further modified by the electrostatic response of the surrounding conductive surfaces (image charge effect). However, the contribution of the image charges is accounted for only on the domain boundaries representing the detector depth, while the effect on the appropriately-chosen wide lateral boundaries is considered negligible and thus omitted. It is worth noting that a carrier is also subject to the influence of its own image charges and therefore the term $\mathbf{E}_{\mathrm{mob}_{i\leftarrow i}}$ is not null. Furthermore, to avoid the problem of singularities arising when the distance between carriers tends to zero, we assume the charge to be uniformly distributed within a sphere of finite radius, which we call de-Broglie radius R_{dB}. Thus, the bare electric field felt by charge q_i due to charge q_j (either real or image charge) can be written as:

$$\mathbf{E}_{i\leftarrow j}(\mathbf{r}_i(t),\mathbf{r}_j(t))=\begin{cases}\frac{q_j}{4\pi\varepsilon_0\varepsilon_{\mathrm{R}}}\frac{\mathbf{r}_i(t)-\mathbf{r}_j(t)}{R_{\mathrm{dB}}^3}, & \text{for } \left|\mathbf{r}_i(t)-\mathbf{r}_j(t)\right|<R_{\mathrm{dB}}\\ \frac{q_j}{4\pi\varepsilon_0\varepsilon_{\mathrm{R}}}\frac{\mathbf{r}_i(t)-\mathbf{r}_j(t)}{\left|\mathbf{r}_i(t)-\mathbf{r}_j(t)\right|^3}, & \text{for } \left|\mathbf{r}_i(t)-\mathbf{r}_j(t)\right|\geq R_{\mathrm{dB}}\end{cases} \tag{2}$$

where ε_0 is the vacuum permittivity and ε_{R} is the dielectric constant of the detector material. The magnitude of the de-Broglie radius can be estimated from quantum-mechanic and thermodynamic arguments (typically referred to as thermal de-Broglie wavelength), and in silicon it is reported to be in the range 5–10 nm at room temperature [21,22]. As a trade-off, we chose 7 nm both for electrons and for holes.

The charge cloud dynamics is solved by tracking the space–time evolution of each single carrier over the total simulation time span. At each simulation time step Δt, the total displacement $\Delta\mathbf{r}_{\mathrm{tot}_i}$ is computed as the vector superposition of a deterministic displacement $\Delta\mathbf{r}_{\mathrm{drift}_i}$ due to the total electric field, obtained by integration of the drift equation:

$$\frac{\mathrm{d}\mathbf{r}_{\mathrm{drift}_i}}{\mathrm{d}t}=\mathbf{v}_i(\mathbf{r}_1(t),\mathbf{r}_2(t),\ldots,\mathbf{r}_N(t)),\quad \forall i=1,\ldots,N \tag{3}$$

where $\mathbf{v}_i$ is the velocity of the ith carrier, with a random displacement $\Delta\mathbf{r}_{\mathrm{dif}_i}$ representing the thermal diffusion. A field-dependent model for the drift mobility was adopted [23]:

$$\mu=\frac{\mu_0}{\left(1+\left(\frac{\mu_0|\mathbf{E}_{\mathrm{tot}}|}{v_{\mathrm{sat}}}\right)^{\beta}\right)^{1/\beta}} \tag{4}$$

where μ represents the overall mobility coefficients for electrons or holes, μ_0 is the low-field value, β is a constant and v_{sat} is the saturation velocity, which, according to [24], can be expressed in silicon as:

$$v_{\mathrm{sat}}=\frac{2.47\cdot 10^7}{1+0.8e^{T/600}}\,\frac{\mathrm{cm}}{\mathrm{s}} \tag{5}$$

where T is the lattice temperature expressed in Kelvin. For the diffusion coefficient D, Einstein relation at lattice temperature was maintained since it is in good agreement with the experimental data up to high fields, at least for silicon [25].

Charge and current signals induced at any desired electrode are computed as the superposition of the contribution of the individual carriers according to Ramo's theorem [26]:

$$Q_{\mathrm{ind}_k}(t) = \sum_{i=1}^{N} -q_i V_{\mathrm{w}_k}(\mathbf{r}_i(t)) \tag{6}$$

$$I_{\mathrm{ind}_k}(t) = \sum_{i=1}^{N} q_i \mathbf{v}_i(t) \cdot \mathbf{E}_{\mathrm{w}_k}(\mathbf{r}_i(t)) \tag{7}$$

where V_{w_k} and $\mathbf{E}_{\mathrm{w}_k}$ are the so-called *weighting* potential and *weighting* field, respectively, of the electrode k.

The electrodes are modeled as idealized rectifying boundaries. Carriers that reach the "wrong" electrode (i.e. electrons approaching the p^+-contact or holes approaching the n^+-contact) due to the intense internal Coulomb interaction and concentration gradients in the first instants after generation are reflected rather than collected and annihilated. This ensures a physically consistent description of possible plasma formation and erosion process and provides excellent agreement with the experimental pulse shapes.

2.2. Numerical methods

The static and weighting fields are computed by means of a 3D Poisson solver based on the iterative Gauss–Seidel method with Successive Over-Relaxation (SOR) on a discretized Cartesian mesh that takes into account the boundary conditions at the surfaces $x = 0$ and $x = d$, where d is the thickness of the detector, and the fixed charge distribution in the fully depleted bulk. In the computation of the time dependent field due to the mutual interaction between carriers, the infinite series of image charges needed to assure homogeneous Dirichlet boundary conditions on both detector's surfaces $x = 0$ and $x = d$ is truncated for simplicity to the first two terms with negligible loss of accuracy.

The non-linear, coupled systems of drift equations giving the deterministic displacement $\Delta\mathbf{r}_{\mathrm{drift}}$ during a simulation time step Δt is solved by a Runge–Kutta 4(5) algorithm with adaptive internal step size controlled by the requested value of tolerance. The intrinsic parallel nature of the problem makes the task ideally suited for vectorized routines available for modern GPUs, where the solver's internal vectorization allows for a simultaneous update of the full state vector. This ensures that the electric fields for all mobile carriers are evaluated at the same temporal instants, maintaining the physical consistency of the interactions throughout the whole simulation time step.

The diffusive displacement $\Delta\mathbf{r}_{\mathrm{dif}}$, on the other hand, is computed by extracting randomly a vector from a 3D Gaussian distribution with standard deviation $\sqrt{2D\Delta t}$, corresponding to the standard deviation due to thermal diffusion over the integration time Δt.

Since the core-routine computing the dynamic electric fields of the mobile carriers is an intensive operation with complexity of $O(N^2)$, two further strategies (beyond parallel calculus) were implemented to keep the computational burden under control. First, the simulation time step Δt is not constant but is adjusted at run-time for each subsequent integration step by imposing a constraint on the maximum displacement $\Delta r_{\mathrm{drift}_{\mathrm{max}}}$ permitted for the carriers. Knowing their initial velocity, this *dynamic time-step algorithm* estimates the statistical distribution of the required time steps over all the carriers and it extracts the chosen value such that a predefined percentile of the carriers fulfills the constraint. In this way, the dynamics of the charge cloud can be followed with high accuracy across virtually any time scale without unnecessary computational effort. Second, the total amount of carriers can be reduced via *clustering* to a smaller, representative set of carriers, where each new carrier has an effective charge greater than the elementary one to compensate for the smaller sample size. The so called *macro charge* M_q factor represents the number of elementary charges q per cluster. To maintain the same charge density within the physical size of a single carrier, the corresponding de-Broglie radius R'_{dB} is scaled as:

$$R'_{\mathrm{dB}} = R_{\mathrm{dB}} \sqrt[3]{M_q} \tag{8}$$

Both strategies were previously validated in [18].

The code was implemented in Python, using Numba [27] for just-in-time (JIT) compilation of performance-critical kernels and the CUDA toolkit provided by the PyTorch [28,29] framework for NVIDIA GPU vectorized operations.

2.3. Case study

As a validation case study we computed the space–time evolution and induced signals of the electron–hole clouds resulting from a bunch of 3,600× and 36,000 × 1 keV photons impinging on a $\mathrm{p}^+\mathrm{nn}^+$ silicon diode under different bias conditions. This case represents the realistic level of ionization expected at pixel level in 2D imaging detectors for the modern FEL X-ray facilities for every X-ray pulse [1]. In silicon, 3600 × 1 keV photons generate 10^6 e–h pairs while 36,000 × 1 keV photons generate 10^7 e–h pairs.

The simulated silicon diode is 280 μm thick with a bulk donor concentration of $8.2 \cdot 10^{11}$ cm^{-3}, corresponding to a depletion voltage of 49 V. In order to evaluate the impact of the applied electric field on the transport properties, we performed simulations with bias voltages $\mathrm{V}_{\mathrm{bias}}$ = 100 V, 200 V and 500 V. We simulated the case of a front injection condition – photons impinging on the p^+ side of the detector – and of a back injection condition – photons impinging on the n^+ side of the detector – since they allow checking and studying the transport properties of electrons and holes independently. Lattice temperature is assumed to be 20 °C. The generated charge of 10^6 and 10^7 e–h pairs have been simulated as N = 20,000 e–h pairs with a macro charge $M_q = 50$, and $M_q = 500$, respectively. The initial electron–hole distributions were generated according to a decaying exponential along the impinging direction x with $\lambda = 3$ μm (approximately the absorption length of 1 keV photons in silicon [30]) while a Gaussian distribution with standard deviation of 10 μm was assumed on the incident surface. The considered injection levels allow probing the detector response and the occurrence of plasma effects at realistic charge densities, namely $\sim 10^{14}$ e–h pairs/cm^{-3} and $\sim 10^{15}$ e–h pairs/cm^{-3}, respectively. The maximum allowed carriers displacement for the dynamic time-step algorithm was $\Delta r_{\mathrm{drift}_{\mathrm{max}}} = 1$ μm, while the time-step Δt could span from a minimum of 10 ps to a maximum of 0.5 ns. The absolute tolerance set for the Runge–Kutta 4(5) algorithm was set 10 nm. Regarding the mobility parameters for electrons and holes β_{e} and β_{h}, respectively, appearing in Eq. (4), we chose for electrons the value $\beta_{\mathrm{e}} = 1$ [25], which was found as a better choice for our case with respect to other references – e.g. [23] reports a $\beta_{\mathrm{e}} = 2$ – while for holes the value $\beta_{\mathrm{h}} = 1$, which seems to be a generally accepted value [23,25].

The simulations were performed on several DECTRIS CLOUD [31] high-performance computing (HPC) nodes, each equipped with an NVIDIA L4 or A10G GPU with 24 GB of VRAM and a compute capability of 8.6. Computation times were strongly coupled to the desired temporal and spatial accuracy and very case-specific, ranging from a few minutes for the simpler scenarios (e.g. p-side injection of 10^6 e–h pairs and with bias voltage of 500 V) to several hours for the most difficult ones (e.g. n-side injection of 10^7 e–h pairs and with bias voltage of 100 V).

Simulation results were compared in terms of induced current pulses to the experimental data extracted from a previous work [20]. There, the 10^6 and 10^7 e–h pairs were generated of the same $\mathrm{p}^+\mathrm{nn}^+$ diode structure previously described by means of a pulses laser with a wavelength of 660 nm, focused with a dedicated optics down to a spot with Gauss distribution with a standard deviation of 10 μm rms. For a correct comparison with the experimental data, simulated currents were convoluted with the pulse response of the readout electronic chain used in [20].

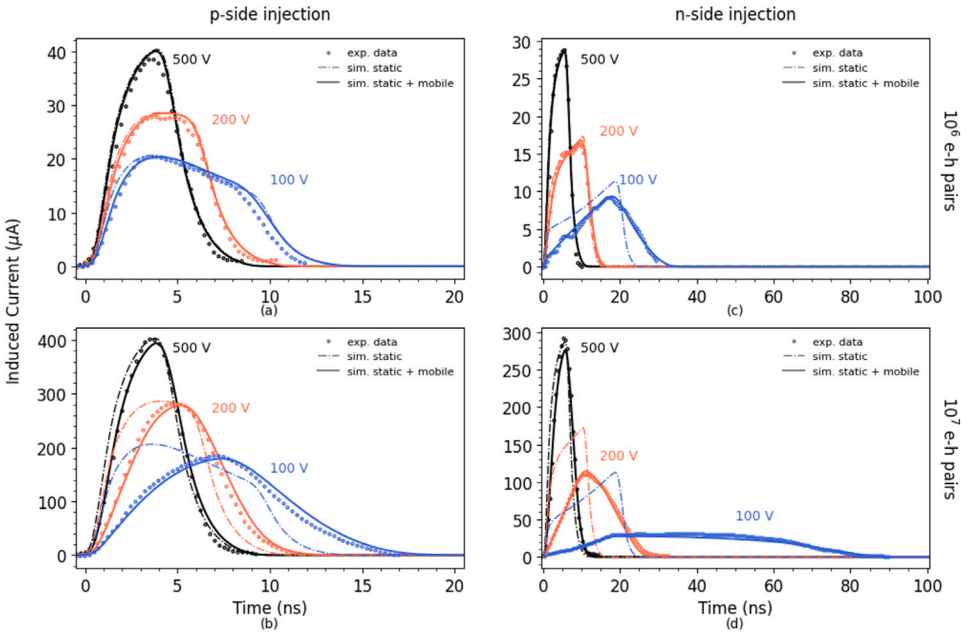

Fig. 1. Experimental and simulated current pulses for different injection conditions and bias voltages. Panels (a) and (b) show p-side injection for 10^6 and 10^7 e–h pairs, respectively. Panels (c) and (d) show n-side injection for 10^6 and 10^7 e–h pairs, respectively. Simulation data are presented both accounting for (solid lines) and neglecting (dashed lines) the mobile charge contribution to the electric field. Experimental data are extracted from [20].

3. Results and discussion

3.1. Induced currents

The comparison between experimental and simulated current pulses for a p-side injection of 10^6 e–h pairs is shown in Fig. 1(a), while of for a p-side injection of 10^7 e–h pairs in Fig. 1(b). Curves are shown for the bias voltages 100 V, 200 V and 500 V. For reference, simulated data are shown both with and without the mobile charge contribution to the electric field. For a charge injection of 10^6 e–h pairs, the discrepancy between simulations with and without the contribution of the mobile carriers to the electric field is almost unnoticeable and both families of curves are in excellent agreement with the experimental data. For a charge injection of 10^7 e–h pairs, on the other hand, the discrepancy between the two simulations regimes is clearly observed, in particular for decreasing bias voltages. In such scenarios, indeed, the reduced static electric field results in longer plasma erosion processes and therefore longer collection times. Hence, including the mobile field contribution is essential to yield excellent agreement between experiments and simulations. As a quantitative measure of the agreement between experimental and simulated results, we chose the L^2 relative error norm (L^2REN), defined as follows:

$$L^2\text{REN} = \sqrt{\frac{\sum_{i=1}^{\text{NoP}} \left(x_i^{\text{exp}} - x_i^{\text{sim}}\right)^2}{\sum_{i=1}^{\text{NoP}} (x_i^{\text{exp}})^2}} \tag{9}$$

where NoP is the number of data points. The L^2REN values for the p-side injection scenario are reported in Table 1. When only the static contribution to the electric field is accounted for, the L^2REN is on the order of 10% in the charge injection of 10^6 e–h pairs case, but it raises up to above 40% in the case of the charge injection of 10^7 e–h pairs and lowest bias voltage. When the contribution of the mobile carriers to the electric field is also accounted for, the L^2REN remains below 10% in all cases.

The comparison between experimental and simulated current pulses for a n-side injection of 10^6 e–h pairs is shown in Fig. 1(c), while of for a n-side injection of 10^7 e–h pairs in Fig. 1(d). Also in this case, the probed bias voltages were 100 V, 200 V and 500 V and simulated data are shown both with and without the mobile charge contribution to the electric field. This side of the diode, opposite to the pn junction, features a lower static electric field with respect to the previous one and sensible plasma effects are already observed at a charge injection of 10^6 e–h pairs and a bias voltage of 100 V, while it becomes macroscopic at a charge injection of 10^7 e–h pairs. In this extreme scenario, accounting for the contribution of the mobile charge to the electric field is critical for an accurate agreement between experiments and simulations. The L^2REN values for the n-side injection scenario are also reported in Table 1. When only the static contribution to the electric field is accounted for, the L^2REN reaches values up to about 160% in the worst case of a charge injection of 10^7 e–h pairs and lowest bias voltage. On the other hand, the L^2REN remains below 13% for the same case, when the contribution of the mobile carriers to the electric field is also accounted for. Furthermore, it should be noted that in this specific high-injection scenario, the experimental signal appears to be generated by a charge quantity approximately 15% higher than the nominal value used in other cases. This experimental discrepancy in the injected charge introduces an additional source of uncertainty that may further impact the accuracy of the comparison between simulations and measurements.

3.2. Charge cloud evolution

To provide a visual insight into the spatio-temporal evolution of the charge cloud at different charge injection levels, we show in Fig. 2 (a–d) and Fig. 2 (e–h) a series of 2D projections taken at different time instants, for a p-side injection of 10^6 e–h pairs and 10^7 e–h pairs, respectively, at the bias voltage of 100 V. At the injection of 10^6 e–h pairs the snapshots corresponds to the time instants $t = 0.5$ ns, $t = 2.5$ ns, $t = 4$ ns and $t = 8$ ns. Holes, represented in red, are quickly collected by the p^+ electrode forming the p^+n-junction at the upper surface ($x = 0$). Electrons, represented in green, move downwards to the n^+ electrode at the bottom surface ($x = 280$ μm) in a rather compact fashion mainly determined by the thermal diffusion rather than mutual Coulomb forces, even at the very beginning of the cloud expansion. The whole charge collection process takes about 11 ns. At the injection of 10^7 e–h pairs the snapshots corresponds to the time

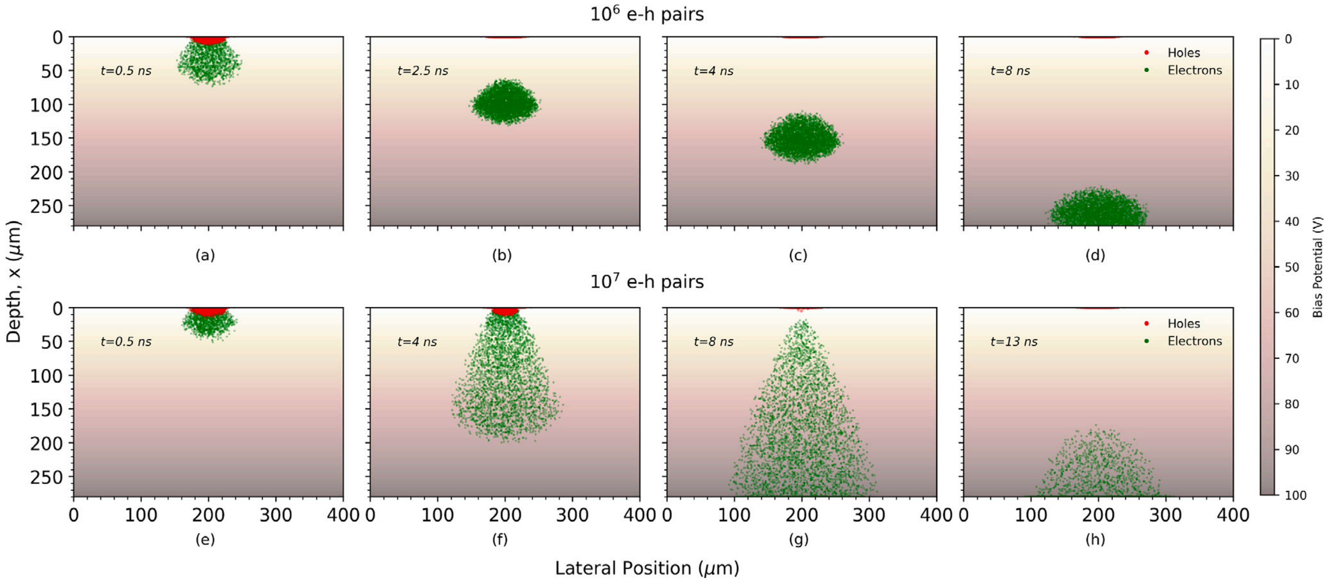

Fig. 2. 2D projections of the 3D charge cloud evolution for a p-side injection at $V_{\mathrm{bias}} = 100$ V. The top row (a–d) shows the 10^6 e–h pairs case at $t = 0.5, 2.5, 4, 8$ ns. The bottom row (e–h) shows the 10^7 e–h pairs case at $t = 0.5, 4, 8, 13$ ns. The p$^+$n-junction is at $x = 0$, while the n$^+$ electrode is at $x = 280$ μm. The static electric potential is shown as a color gradient.

Table 1
Comparison of the L^2 Relative Error Norm (L^2REN) between experimental data and simulations for both p-side and n-side injections. The "Static" model accounts only for the static electric field, while the "Full" model includes mobile carrier contributions.

Injection	e–h pairs	Bias (V)	L^2REN (Static)	L^2REN (Full)
p-side	10^6	100	12.4%	9.3%
		200	7.8%	5.4%
		500	9.5%	6.9%
	10^7	100	43.4%	8.8%
		200	26.5%	7.9%
		500	11.8%	5.5%
n-side	10^6	100	46.7%	6.4%
		200	11.6%	8.1%
		500	10.1%	7.4%
	10^7	100	158.6%	12.7%
		200	89.7%	6.4%
		500	23.6%	7.1%

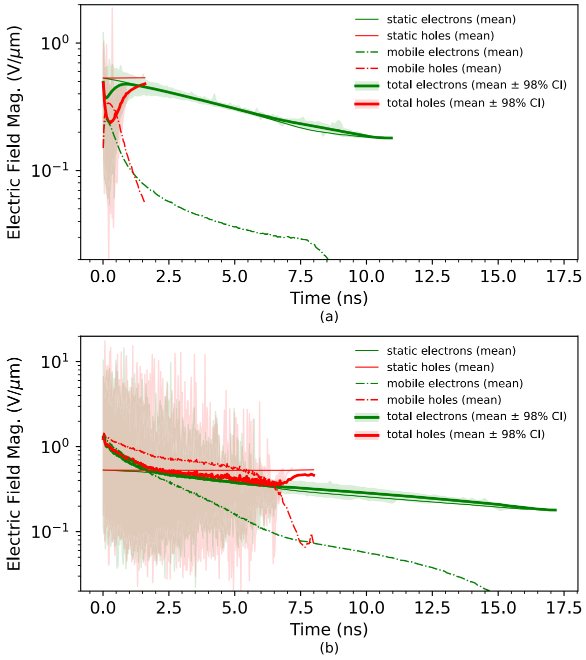

Fig. 3. Magnitude of the static component, of the mobile carriers component and of the total electric fields averaged over the electrons population (green) and holes population (red), for a p-side injection of 10^6 e–h pairs (a) and 10^7 e–h pairs (b) at $V_{\mathrm{bias}} = 100$ V.

instants $t = 0.5$ ns, $t = 4$ ns, $t = 8$ ns and $t = 13$ ns and the situation changes sensibly. Indeed, the charges form a plasma region which, shielding the core, prevents a prompt separation of electrons and holes by the static electric field. Electrons, slowly carried away from the plasma zone, form a long tail toward the back electrode with increased spatial broadening both in the longitudinal and in the lateral direction. The whole collection process takes now about 18 ns.

3.3. Electric fields analysis

To shed light on the complexity of the forces acting on the carriers during the collection process, we show in Fig. 3 the *average* magnitude of the static, mobile and total components of the electric field for electrons and holes, as a function of time and for p-side injections of 10^6 e–h pairs (a) and 10^7 e–h pairs (b) at the bias voltage of 100 V. In the first case, the static component dominates on the mobile one for both electrons and holes over the entire temporal range, even though in the first instants, and until roughly 1.5 ns, the total electric fields exhibit a slight depression, symptom of a minor onset of plasma effect. The large confidence intervals around the mean values are due to the inherent local nature of the space-charge effects (screening or enhancement), which affects each carrier differently depending on its instantaneous position within the cloud. In the second, more extreme case, the mobile component exceeds the static one for both electrons and holes, until about 1.5 ns and 5.5 ns, respectively, leading to a major onset of plasma effect. Before the crossover point at about 1.5 ns, the average magnitude of the total field acting on the electrons follows the mobile component, indicating a Coulomb interaction-driven evolution dynamics, while afterwards it follows the static component, as a consequence of the electrons being progressively released from the

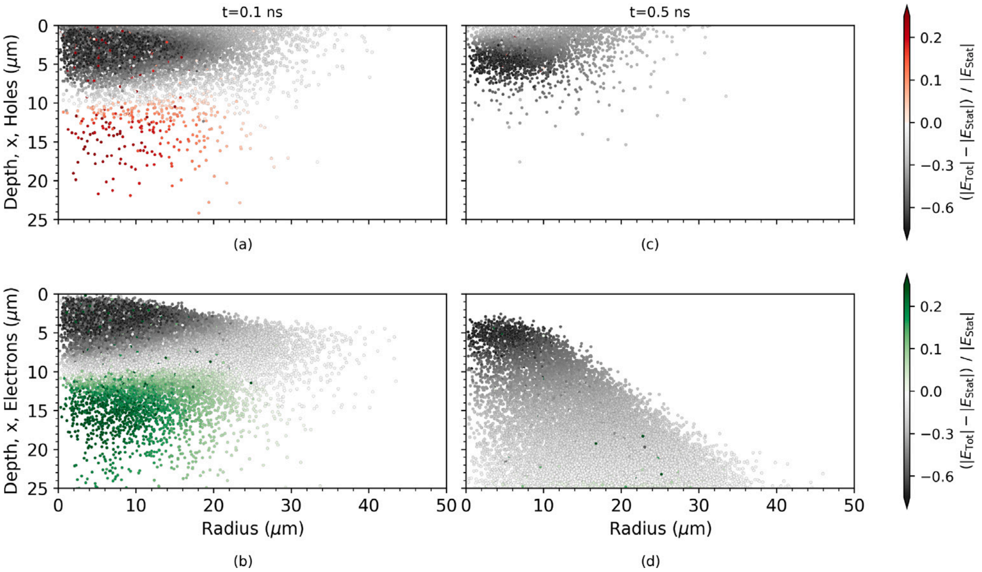

(a) (c)

(b) (d)

Fig. 4. Spatial distribution of holes (a)(c) and electrons (b)(d) for a p-side injection of 10^6 e–h pairs, at $V_{\text{bias}} = 100$ V and at the selected time instants $t = 0.1$ ns (a)(b) and $t = 0.5$ ns (c)(d). The horizontal axis represents the radial coordinate, where the origin marks the symmetry axis of the charge cloud, while the vertical axis indicates the depth within the detector. The color code represents the relative difference between the magnitude of the total electric field and the magnitude of the static electric field acting on each single carrier. For reference, the p^+n-junction is at $x = 0$.

plasma zone and drifting freely towards their collecting n^+ electrode. For the holes the situation is seemingly different. During basically all their lifetime, the average magnitude of the total electric field results lower than the mobile contribution, suggesting that the net vectorial contribution is acting against the static field. This causes in general a lengthening of the collection process of the holes towards the p^+ electrode and, consequently, a slower release of the electrons from the plasma zone. Again, the large confidence intervals are indicative of the inherent locality of space-charge effects.

With the help of Fig. 4 and Fig. 5, we can deepen the understanding of the impact of the space-charge distribution on the electric fields acting on the individual carriers.

Fig. 4 shows the spatial distribution of holes (a)(c) and electrons (b)(d) for p-side injection of 10^6 e–h pairs, a bias voltage of 100 V, at the selected time instants $t = 0.1$ ns (a)(b) and $t = 0.5$ ns (c)(d). The horizontal axis represents the radial coordinate, where the origin marks the symmetry axis of the charge cloud, while the vertical axis indicates the depth within the detector. The color code represents the relative difference between the magnitude of the total electric field and the magnitude of the static electric field acting on the represented carrier. Let us recall that, in the plot, holes drift upwards while electrons downwards. Despite the corresponding current pulse in Fig. 1(a) shows no significant distortions due to plasma effects, a refined analysis can still capture its subtle onset. The charge distributions can indeed be conceptually subdivided into distinct sub-regions, each characterized by a specific electric field regime. Specifically, the cloud cores correspond to the main overlapping region between holes and electrons, where the magnitude of the total electric field is depressed due to the electrostatic shielding typical of an incipient plasma effect (gray region, color code negative). Moving towards the boundaries of these cores, a transition region emerges. Here, carriers are primarily subject to the static field component, which progressively erodes the clouds. In contrast, the outer region (colored region, color code positive) at the bottom of the cloud visible only at $t = 0.1$ ns is dominated by mutual Coulomb interactions driven by the higher concentration of electrons relative to holes and the net positive charge induced by the carriers on the contact at $x = d$. Within this regime, the outermost electrons are pushed downwards while holes are slightly dragged upwards by the resulting overall electrostatic forces.

Fig. 5 shows, instead, the spatial distribution of holes (a)(c) and electrons (b)(d) for p-side injection of 10^7 e–h pairs, a bias voltage of 100 V, at the selected time instants $t = 0.5$ ns (a)(b) and $t = 4$ ns (c)(d). In this case, the corresponding current pulse in Fig. 1(b) exhibits considerable distortions due to pronounced plasma effects. At $t = 0.5$ ns, unlike the previous case, the charge distributions feature an innermost core where carriers are subject to intense Coulomb interactions that bind holes and electrons together. Upon further inspection, these forces exhibit a dominant vertical component directed downwards for holes and upwards for electrons, attributable not only to the self-repulsive force but also to the attractive force of the image charges relative to the mirror plane at $x = 0$. This interaction is particularly critical in the initial stages of the plasma evolution, where proximity to the injection electrode enhances electrostatic binding, delaying carrier separation beyond the predictions of simpler models. Simultaneously, in the outer regions of the core, the total electric field magnitude is depressed due to electrostatic shielding. Consequently, electrons are swept toward the collecting electrode only at the core boundaries. Furthermore, the Coulomb forces acting downwards and outwards on the electron tail result in a spatial spread substantially greater than that expected from purely thermal diffusion. At $t = 4$ ns, the core cloud is still held together by mutual Coulomb interactions. However, given the progressively reduced charge density and the increasing distance from the upper boundary, these forces are essentially isotropic. This electrostatic binding effectively delays carrier separation, resulting in the characteristic "plasma delay" observed in the current pulse, where the peak is shifted and the pulse duration is significantly extended.

This separation of the field components allows for a deeper interpretation of the plasma dynamics, providing a refined perspective compared to classical phenomenological models. In the work by Tove and Seibt [6], the plasma core is described as a region where the external electric field is effectively canceled – and thus vanishes – due to the formation of polarized charge sheaths. While this "zero-field" approximation explains why the cloud effectively shields itself from the external extraction field, our simulations reveal the complex microscopic forces that sustain this state. As shown in Fig. 5, although the

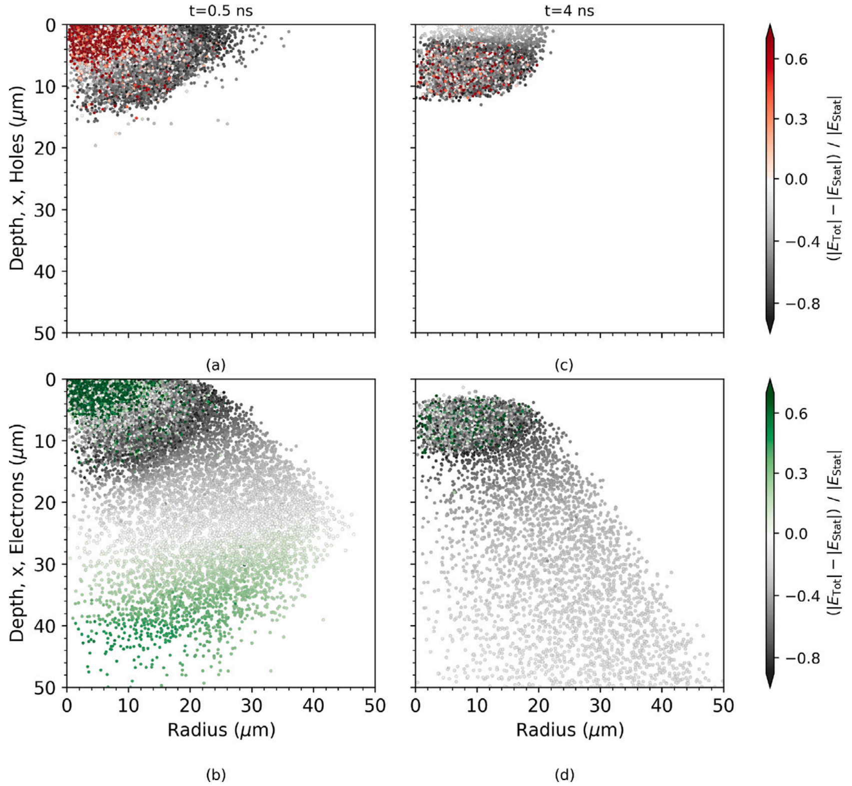

Fig. 5. Spatial distribution of holes (a)(c) and electrons (b)(d) for p-side injection of 10^7 e–h pairs, a bias voltage of 100 V and at the selected time instants $t = 0.5$ ns (a)(b) and $t = 4$ ns (c)(d). The horizontal axis represents the radial coordinate, where the origin marks the symmetry axis of the charge cloud, while the vertical axis indicates the depth within the detector. The color code represents the relative difference between the magnitude of the total electric field and the magnitude of the static electric field acting on each single carrier. For reference, the p$^+$n-junction is at $x = 0$.

net field at the inner boundary of the cores is significantly depressed, the individual carriers in the inner core are far from being in a passive state. On the contrary, they are subjected to intense local Coulomb interactions that effectively bind holes and electrons together. In this high-interaction zone, the longitudinal coupling with image charges at the mirror plane further anchors the carriers to the injection site. This internal binding mechanism provides the physical basis for the shielding effect: the carriers remain "locked" in a neutral-like state, resisting the erosion process until the density decreases sufficiently for the external field to finally penetrate and prevail.

4. Conclusion

We developed a Monte Carlo simulation code for the self-consistent computation of the electron–hole dynamics and signal formation in 3D semiconductor radiation detectors. The adopted multi-body approach tracks the spatio-temporal evolution of the charge cloud on a individual carrier basis, including the mutual Coulomb interactions necessary to accurately model space-charge effects. The architecture leverages on the vectorized calculus capabilities of modern GPUs. Dedicated numerical strategies, i.e. charge clustering and dynamic time-step algorithm, were implemented to maintain high accuracy without compromising on the computational effort.

We carried out a set of simulations for the case study of a p$^+$nn$^+$ silicon diode irradiated by 1 keV photons under different bias and charge injection conditions – up to 10^7 e–h pairs – since it realistically represents the challenging operating conditions at X-ray facilities e.g. FELs. The chosen case study allowed comparison of simulation results with experimental data from a previous work, showing an excellent agreement in all the considered cases despite the occurrence of strong plasma effects. The phenomenology of the plasma effect was presented at microscopic level, revealing how discrete carrier-carrier interactions and image-charge forces govern the spatio-temporal evolution of the track especially during the first instants. This self-consistent multi-body approach explains the physical origin of the plasma delay and provides a robust framework for predicting detector response non-linearities in high charge-injection scenarios.

CRediT authorship contribution statement

Pietro Zambon: Writing – review & editing, Writing – original draft, Visualization, Validation, Software, Methodology, Investigation, Conceptualization. **Filippo Buda:** Writing – review & editing, Validation, Software, Methodology. **Chiara Guazzoni:** Writing – review & editing, Validation, Supervision, Conceptualization. **Andrea Castoldi:** Writing – review & editing, Writing – original draft, Validation, Supervision, Software, Resources, Methodology, Investigation, Conceptualization.

Declaration of competing interest

The authors declare the following financial interests/personal relationships which may be considered as potential competing interests: Author P. Z. is an employee of DECTRIS Ltd. The simulation tool and the computing resources described in this work were used solely for research purposes; DECTRIS Ltd. declares no financial or commercial interests in the software itself or in the results of this study. The code is not available as a commercial product, and the use of the internal cloud infrastructure did not involve any commercial transaction or financial conflict. The remaining authors declare no competing interests.

Acknowledgments

The authors would like to thank M. Burian and F. Eisenstein for their technical assistance in configuring the computing nodes used for the simulations. We also acknowledge DECTRIS Ltd. for providing access to internal high-performance computing (HPC) resources through the DECTRIS CLOUD infrastructure, which were made available exclusively for the scientific purposes of this research without any financial contribution to the project.

Data availability

Data will be made available on request.

References

[1] J. Becker, D. Eckstein, R. Klanner, G. Steinbrück, Impact of plasma effects on the performance of silicon sensors for X-ray free-electron lasers, Nucl. Instruments Methods A 615 (2010) 230–236, http://dx.doi.org/10.1016/j.nima.2010.01.082.

[2] A. Castoldi, C. Guazzoni, T. Parsani, F. Riccio, P. Zambon, C. Boiano, L. Carraresi, F. Taccetti, L. Acosta, G. Cardella, T. Minniti, G. Verde, L. Quattrocchi, A. Trifirò, Experimental investigation of the impact of inter-strip incidence on the signal shape in double sided silicon strip detectors for particle identification, in: 2013 IEEE Nuclear Science Symposium and Medical Imaging Conference Record, NSS/MIC, 2013, http://dx.doi.org/10.1109/NSSMIC.2013.6829489.

[3] J. Apostolakis, M. Bandieramonte, S. Banerjee, N. Bartosik, G. Corti, G. Cosmo, V.D. Elvira, T. Evans, A. Gheata, S. Pagan Griso, V. Ivantchenko, C. Jones, M. Klute, C. Leggett, B. Morgan, T. Novak, K. Pedro, H. Paganetti, Detector simulation challenges for future accelerator experiments, Front. Phys. 10 (2022) 913510, http://dx.doi.org/10.3389/fphy.2022.913510.

[4] E. Currás, M. Fernandez, M. Moll, Gain suppression mechanism observed in low gain avalanche detectors, Nucl. Instruments Methods A 1031 (2022) 166530, http://dx.doi.org/10.1016/j.nima.2022.16653.

[5] M.C. Jiménez-Ramos, J. García López, A. García Osuna, I. Vila, E. Currás, R. Jaramillo, S. Hidalgo, G. Pellegrini, Study of ionization charge density-induced gain suppression in LGADs, Sensors 22 (3) (2022) 1080, http://dx.doi.org/10.3390/s22031080.

[6] P.A. Tove, W. Seibt, Plasma effects in semiconductor detectors, Nucl. Instrum. Methods 51 (1967) 261–269, http://dx.doi.org/10.1016/0029-554X(67)90012-2.

[7] A. Alberigi Quaranta, A. Taroni, G. Zanarini, Plasma time in semiconductor detectors, IEEE Trans. Nucl. Sci. 15 (3) (1968) http://dx.doi.org/10.1109/TNS.1968.4324961.

[8] W. Seibt, K.E. Sundström, P.A. Tove, Charge collection in silicon detectors for strongly ionizing particles, Nucl. Instrum. Methods 113 (1973) 317–324, http://dx.doi.org/10.1016/0029-554X(73)90496-5.

[9] D. Pfeiffer, L. De Keukeleere, C. Azevedo, F. Belloni, S. Biagi, V. Grichine, et al., Interfacing geant4, garfield++ and degrad for the simulation of gaseous detectors, Nucl. Instrum. Methods Phys. Res. Sect. A 935 (2019) 121–134, http://dx.doi.org/10.1016/j.nima.2019.04.110.

[10] S. Spannagel, K. Wolters, D. Hynds, N. Alipour Tehrani, M. Benoit, D. Dannheim, N. Gauvin, A. Nürnberg, P. Schütze, M. Vicente, Allpix2: a modular simulation framework for silicon detectors, Nucl. Instrum. Methods Phys. Res. Sect. A Accel. Spectrom. Detect. Assoc. Equip. 901 (2018) 164–172, http://dx.doi.org/10.1016/j.nima.2018.06.020.

[11] Sentaurus Device user manual, https://www.synopsys.com.

[12] Silvaco Atlas user manual, https://silvaco.com.

[13] M. Pinson, P. Caron, Transient current simulations: benchmark of numerical tools for proton, electron, and alpha irradiation in solid-state detectors, IEEE Trans. Nucl. Sci. 70 (2023) 8, http://dx.doi.org/10.1109/TNS.2023.3245402.

[14] S. Boorboor, S.A.H. Feghhi, H. Jafaria, Efficient modeling of plasma effect on the signal formation in planar silicon detectors, Eur. Phys. J. C 85 (2025) 1281, http://dx.doi.org/10.1140/Epjc/S10052-025-14934-Z.

[15] S. Pape, M. Moll, M. Fernández García, M. Wiehe, TCAD simulation of two photon absorption—Transient current technique measurements on silicon detectors and LGADs, Sensors 24 (2024) 8032, http://dx.doi.org/10.3390/s24248032.

[16] X. Xie, A. Bergamaschi, M. Brückner, M. Carulla, R. Dinapoli, S. Ebner, K. Ferjaoui, V. Gautam, D. Greiffenberg, S. Hasanaj, J. Heymes, V. Hinger, V. Kedych, T. King, S. Li, C. Lopez-Cuenca, A. Mazzoleni, D. Mezza, K. Moustakas, A. Mozzanica, M. Müller, J. Mulvey, K.A. Paton, C. Ruder, B. Schmitt, P. Sieberer, S. Silletta, D. Thattil, J. Zhang, E. Fröjdh, Optimization and validation of charge transport simulation for hybrid pixel detectors incorporating the repulsion effect, Nucl. Instrum. Methods Phys. Res. A 1081 (2026) 170894, http://dx.doi.org/10.1016/j.nima.2025.170894.

[17] A. Castoldi, E. Gatti, Fast tools for 3-d design problems in semiconductor detectors, Nucl. Instrum. Methods Phys. Res. A 377 (1996) 381–386, http://dx.doi.org/10.1016/0168-9002(96)00020-4.

[18] A. Castoldi, C. Guazzoni, P. Zambon, A 3-D simulation code of electron–hole transport and signal formation with coulomb repulsion and thermal diffusion in 2-D semiconductor detectors, in: 2012 IEEE Nuclear Science Symposium and Medical Imaging Conference Record, NSS/MIC, http://dx.doi.org/10.1109/NSSMIC.2012.6551249.

[19] A. Castoldi, P. Zambon, Simulation of the 3-D Coulomb explosion of the electron–hole distribution at high injection levels in 2-D semiconductor detectors, in: 2013 IEEE Nuclear Science Symposium and Medical Imaging Conference, 2013 NSS/MIC, http://dx.doi.org/10.1109/NSSMIC.2013.6829567.

[20] J. Becker, K. Gärtner, R. Klanner, R. Richter, Simulation and experimental study of plasma effects in planar silicon sensors, Nucl. Instruments Methods Phys. Res. A 624 (2010) 716–727, http://dx.doi.org/10.1016/j.nima.2010.10.010.

[21] A. Sacchetti, Electrical current in nanoelectronic devices, Phys. Lett. A 374 (2010) 4057–4060, http://dx.doi.org/10.1016/j.physleta.2010.08.001.

[22] S.M. Sze, K.K. Ng, Physics of Semiconductor Devices, fourth ed., Wiley, Hoboken, NJ, USA, ISBN: 978-1-119-42911-1, 2021.

[23] D.M. Caughey, R.E. Thomas, Carrier mobilities in silicon empirically related to doping and field, Proc. IEEE 55 (12) (1967) http://dx.doi.org/10.1109/PROC.1967.6123.

[24] S.A. Schwarz, S.E. Russek, Semi-empirical equations for electron velocity in silicon: Part II—MOS inversion layer, IEEE Trans. Electron Devices 30 (12) (1983) http://dx.doi.org/10.1109/T-ED.1983.21424.

[25] C. Jacoboni, C. Canali, G. Ottaviani, A. Alberigi Quaranta, A review of some charge transport properties of silicon, Solid-State Electron. 20 (2) (1977) 77–89, http://dx.doi.org/10.1016/0038-1101(77)90054-5.

[26] S. Ramo, Currents induced by electron motion, Proc. I.R.E. 27 (9) (1939) 584–585, http://dx.doi.org/10.1109/JRPROC.1939.228757.

[27] S.K. Lam, A. Pitrou, S. Seibert, Numba: A python compiler for JIT specialized numerical functions, in: Proc. 2nd Workshop on LLVM Compiler Infrastructure in HPC, 2015, pp. 1–6, http://dx.doi.org/10.1145/2833157.2833162.

[28] A. Paszke, et al., Pytorch: An imperative style, high-performance deep learning library, Adv. Neural Inf. Process. Syst. 32 (2019) 8024–8035.

[29] R.T.Q. Chen, et al., Neural ordinary differential equations, Adv. Neural Inf. Process. Syst. 31 (2018) http://dx.doi.org/10.5555/3327757.3327764.

[30] J.H. Hubbell, S.M. Seltzer, Tables of X-ray Mass Attenuation Coefficients and Mass Energy-Absorption Coefficients (version 1.4), National Institute of Standards and Technology, Gaithersburg, MD, 2004, http://physics.nist.gov/xaamdi.

[31] https://www.dectris.cloud/.